Superconducting and Fermi Surface Properties of a Valence Fluctuation Compound CeIr 2

Kazuyuki Omasa, Takuya Komoda, Yusuke Nakamura, Eiichi Matsuoka, Hisashi Kotegawa, Hideki Tou, Takahiro Sakurai, Hitoshi Ohta, Ai Nakamura, Yoshiya Homma, et al.

Superconducting and Fermi Surface Properties of Valence Fluctuation Compound $CeIr_2$

Kazuyuki Omasa[1], Takuya Komoda[1], Yusuke Nakamura[1], Eiichi Matsuoka[1], Hisashi Kotegawa[1], Hideki Tou[1], Takahiro Sakurai[2], Hitoshi Ohta[1, 3], Ai Nakamura[4], Yoshiya Homma[4], Dai Aoki[4], Daisuke Satoh[5], Mitsuhiro Yoshida[6], Sanu Mishra[7], Ilya Sheikin[7], Hisatomo Harima[1], and Hitoshi Sugawara[1*].

[1] *Graduate School of Science, Kobe University, Kobe 657-8501, Japan*
[2] *Research Facility Center for Science and Technology, Kobe University, Kobe 657-8501, Japan*
[3] *Molecular Photoscience Research Center, Kobe University, Kobe 657-8501, Japan*
[4] *Institute for Materials Research, Tohoku University, Oarai, Ibaraki 311-1313, Japan*
[5] *Research Institute for Measurement and Analytical Instrumentation, AIST, Tsukuba 305-8568, Japan*
[6] *Accelerator laboratory, KEK, Tsukuba 305-0801, Japan*
[7] *Laboratoire National des Champs Magnétiques Intenses (LNCMI-EMFL), CNRS, UGA, 38042 Grenoble, France*

(Received)

To investigate the superconducting and the electronic properties of $CeIr_2$ which was reported as a valence fluctuation compound with the superconducting transition temperature of T_c ~0.3 K, we measured the electrical resistivity, the magnetic susceptibility, and the de Haas-van Alphen (dHvA) effect at low temperatures down to ~30 mK and in high magnetic fields up to 36 T. The upper critical field $\mu_0 H_{c2}$ = 0.23 T determined by the electrical resistivity under the magnetic field as well as the electron–phonon coupling constant λ_{ep} = 0.39 estimated from the Debye temperature suggest that the superconductivity is a weak-coupling BCS-type. The dHvA effect measurements mapped the Fermi surface in detail, in which the dHvA branches with the frequencies of F = (122 ~ 2180) T and the effective masses of m_c^* = (0.83~2.4)m_0 (m_0: rest mass of an electron) were observed, which were reasonably well explained by the band structure calculation based on a full potential linearized augmented-plane-wave (FLAPW) method within the local density approximation (LDA).

1. Introduction

Rare-earth intermetallic compounds RX_2 (R: rare earth element, X: transition metal element) crystallize into the cubic Laves-phase structure ($MgCu_2$-type, $Fd\bar{3}m$, No. 227).[1] Most of the RX_2 compounds with non-magnetic R (Sc, Y, and La) become superconductor, while those with magnetic R (Nd, Pr, and Gd) show ferromagnetism at low temperatures. The several cerium-based CeX_2 compounds, such as $CeCo_2$, $CeRu_2$, $CeRh_2$ and $CeIr_2$, are known to have a non-magnetic ground state and no crystalline field effect. In other words, these materials are classified as valence fluctuation compounds. Among them, $CeIr_2$ is known to exhibit a weakly enhanced Sommerfeld coefficient γ = (20~28) mJ/K^{2}mol, and confirmed the bulk superconductivity below T_c ~0.3 K.[2, 3] Thus, the role of 4*f*-electorn's contribution to the superconductivity is of a great interest such as a possible unconventional superconductivity. Besides its scientific interest, $CeIr_2$ recently attracted much attention as a particularly suitable material for photocathodes because of its high quantum efficiency.[4] However, its detailed physical properties have not been reported so far because of the difficulty in growing high-quality single-crystals. It is essential to study its electronic state to understand both the physical properties and the origin of the good performance for the application.

It is only very recently that we succeeded in growing high-quality single-crystals of $CeIr_2$ and investigated the electrical resistivity and the specific heat.[3] However, the detailed superconducting properties were not investigated because of the relatively low T_c. We also succeeded in observing the de Haas-van Alphen (dHvA) oscillations for the first time in magnetic fields below 17 T. However, only one weakly angular-dependent dHvA frequency branch was observed, while band-structure calculations predicted rather

complex Fermi surfaces with many orbits.[3, 5] In this work, we measured the electrical resistivity, the magnetic susceptibility, and the de Haas-van Alphen (dHvA) effect at temperatures lower and at magnetic fields higher than those of our previous works using the high-quality single-crystals. The experimental results are compared with the band-structure calculation based on a full potential linearized augmented-plane-wave (FLAPW) method within the local density approximation (LDA).

2. Experimental Details

Single-crystals of $CeIr_2$ and the reference compound $LaIr_2$ were grown by a

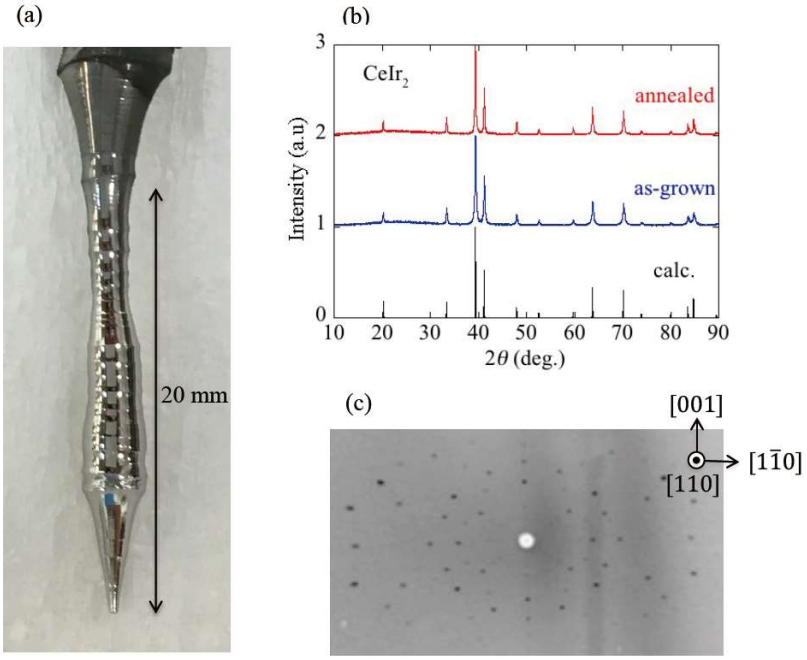

Fig. 1. (Color online) (a) Photograph of single-crystal ingot of $CeIr_2$. (b) Comparison of powder X-ray diffraction patterns between as-grown and annealed samples, which are well explained by the simulation (calc.). (c) Typical back-reflection Laue photograph for [110] direction.

Czochralski pulling method by the tetra-arc furnace as described in previous reports.[3, 6] Most of the samples used in the experiments were annealed at 900 ℃ under the high vacuum, but for the superconducting properties, the as-grown samples were used to avoid the effect of filament superconducting impurity phase as described later. Figure 1(a) shows a photograph of typical single-crystal of $CeIr_2$. The phase purity was confirmed by the powder X-ray diffraction as shown in Fig. 1(b). We note that no impurity phase was detected in both as-grown and annealed samples within the experimental accuracy. The lattice constants of $CeIr_2$ and $LaIr_2$ determined by the single-crystal X-ray diffraction were 7.5807(4) and 7.6936(3) Å, respectively, which were consistent with the previous report.[1] The crystallographic axes of the samples were confirmed by a back-reflection Laue method as shown in Fig. 1(c). The electrical resistivity was measured by a conventional four-probe DC method in a top-loading dilution refrigerator cooled down to ~30 mK with a 15 T superconducting magnetic. We also utilized the four-probe AC method for the electrical resistivity measurement in an adiabatic demagnetization refrigerator down to 0.17 K under zero field, whose results were basically the same as that of the DC one. The magnetic susceptibility was measured by a pulling method in a superconducting quantum interference device (SQUID) magnetometer (Quantum Design, MPMS). The dHvA signals were measured by a standard field-modulation method in a top-loading dilution refrigerator cooled down to ~30 mK with a 15 T superconducting magnetic, and also measured by a magnetic-torque method using a capacitive cantilever at low temperatures down to ~50 mK using a top-loading dilution refrigerator in static magnetic fields up to 36 T at Laboratoire National des Champs Magnétiques Intenses (LNCMI) in Grenoble.

3. Results and Discussion

Figure 2(a) shows the temperature dependences of the electrical resistivity $\rho(T)$ in both as-grown and annealed samples of $CeIr_2$ for the current along the crystal axis J // [100]. These results above 0.5 K are basically the same as the previous report.[3] $\rho(T)$s in both samples decrease with decreasing temperature from room temperature exhibiting

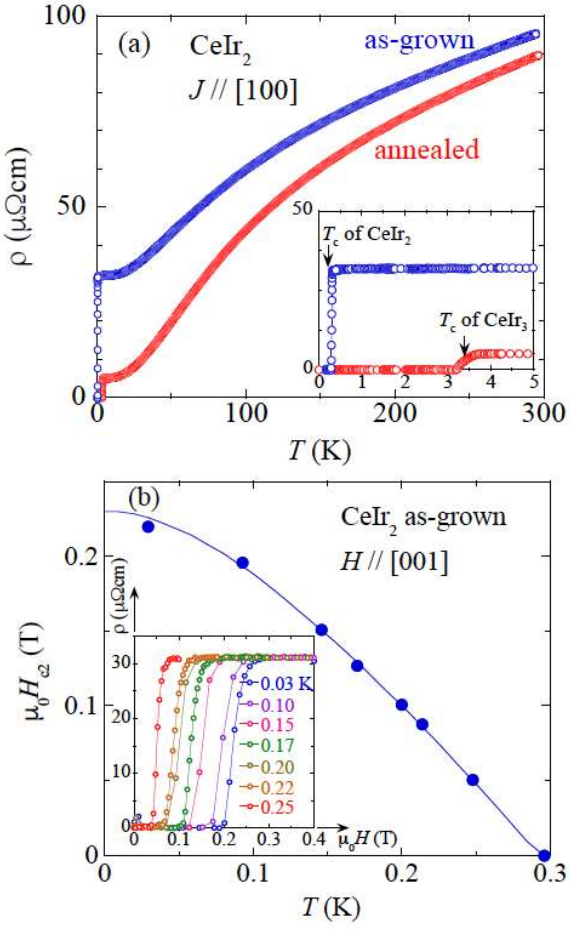

Fig. 2. (Color online) (a) Temperature dependences of electrical resistivity ρ at zero field both for as-grown and annealed samples in $CeIr_2$. The inset shows the expanded view below 5 K. (b) Temperature dependence of the upper critical field in as-grown sample. The solid line shows a fitting of the data based on the WHH model. The inset shows the field dependences of ρ at selected temperatures below 0.25 K.

convex curvature. Below ~15 K, $\rho(T)$s follow T^2-dependence followed by the saturating tendency below ~7 K. Assuming the relation $\rho(T) = \rho_0 + AT^2$ between 4 and 15 K, where ρ_0 is the residual resistivity and A is the coefficient of electron–electron scattering, we can estimate ρ_0 and A to be 32 (5.1) μΩcm and 2.5 (3.5) × 10^{-3} μΩcm/K^2 for as-grown (annealed) sample, respectively. These A-values follow the Kadowaki–Woods relation,[7] considering the Sommerfeld coefficient γ = (20~28) mJ/(K^2mol). The residual resistivity ratio (RRR = ρ_{297K}/ρ_0) of as-grown sample is 3, while that of annealed one is 18.

As shown in the inset of Fig. 2(a), $\rho(T)$ in annealed samples in $CeIr_2$ show superconductivity below ~3.5 K, however, the superconductivity is not a bulk property; the superconductivity was suspected to be caused by filaments or traces of another phase, most probably $CeIr_3$ which was precipitated by annealing.[3, 8] Similar annealing effect was also observed in the reference compound $LaIr_2$ (not shown here); the filament superconductivity of $LaIr_3$ was observed at ~2.5 K in annealed sample while the bulk superconductivity in $LaIr_2$ was observed at ~0.42 K.[6, 9]

To avoid the effect of impurity phase, we measured $\rho(T)$ in as-grown sample at temperatures down to ~30 mK and observed the intrinsic superconducting transition of $CeIr_2$ at T_c = 0.3 K, which is defined as the midpoint of resistivity drop. The transition temperature is consistent with that determined by the specific heat measurement.[3] Combined with the Debye temperature $\Theta_D = 232$ K determined by the specific heat measurement, the electron-phonon coupling constant λ_{ep} can be estimated using a McMillan formula $T_c = \frac{\Theta_D}{1.45}\exp\left[\frac{1.04(1+\lambda_{ep})}{\lambda_{ep}-\mu^*(1+0.62\lambda_{ep})}\right]$ or more conveniently $\lambda_{ep} =$

$\frac{1.04+\mu^{*}\ln(\Theta_D/1.45T_c)}{(1-0.62\mu^{*})\ln(\Theta_D/1.45T_c)-1.04}$,[10] where μ^{*} represents a Coulomb repulsion constant. Assuming a typical value of $\mu^{*}=0.13$, we estimated $\lambda_{ep}=0.39$, which indicates that the superconductivity of $CeIr_2$ is situated in a weak coupling regime.

In order to construct the superconducting *H*–*T* phase diagram, we measured the field dependence of the electrical resistivity at selected temperatures below 0.25 K for *J* // [100] and *H* // [001] as shown in the inset of Fig.2(b), where the superconducting upper critical field $\mu_0 H_{c2}$ was defined as the midpoint of resistivity drop. The main panel of Fig.2(b) shows the *H*-*T* phase diagram. $\mu_0 H_{c2}$ at the lowest temperature of 0.03 K is determined as $\mu_0 H_{c2}$ ~0.22 T, from which we can estimate the coherence length ξ ~390 Å using the relation $H_{c2}=\frac{\Phi_0}{2\pi\mu_0\xi^2}$. From our previous work,[3] the mean free path ℓ was estimated to be $\ell\sim$1080 Å, therefor the superconductivity can be considered within the clean limit ($\ell > \xi$). As the origin of the critical field, two pair-breaking mechanisms are known within the weak-coupling BCS theory, namely, the orbital depairing and the paramagnetic effect. The orbital critical field $\mu_0 H_{orb}$ can be evaluated based on the Werthamer–Helfand–Hohenberg (WHH) model.[11, 12] The model well fits the observed data, and yields the critical field at 0 K $\mu_0 H_{orb}(0) = 0.727\ T_c\ (-d\ \mu_0 H_{c2}/dT)_{T=Tc} = 0.23$ T in the clean limit. On the other hand, the Pauli limit $\mu_0 H_P$ due to the paramagnetic effect is estimated to be $\mu_0 H_P(0) = 1.83\ T_c = 0.54$ T, which is more than two times larger than that of the observation. These facts suggest that the critical field of $CeIr_2$ is governed by the orbital limit rather than by the Pauli limit.

Here after we used the annealed samples for the measurements of normal state

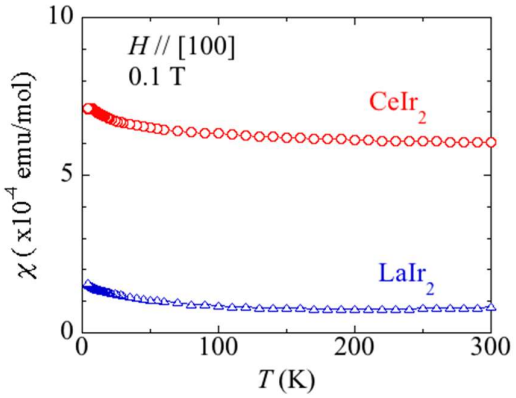

Fig. 3. (Color online) Temperature dependences of magnetic susceptibility χ under the magnetic field of 0.1 T for field along [100] in $CeIr_2$ and $LaIr_2$.

physical properties because of the better sample qualities. Figure 3 shows temperature dependences of magnetic susceptibility $\chi(T)$s in both $CeIr_2$ and $LaIr_2$ under the magnetic field $\mu_0 H$ = 0.1 T for field along H // [100]. Both magnetic susceptibilities are almost independent to the temperature especially at high temperatures, indicating Pauli paramagnetism of these compounds. The slight increasing of $\chi(T)$ with decreasing temperature in both samples is most probably due to the paramagnetic impurity effect. By subtracting the Curie-like contributions, we estimate the Pauli paramagnetic susceptibilities χ_P for $CeIr_2$ and $LaIr_2$ to be 5.9×10^{-4} and 0.71×10^{-4} emu/mol, respectively. The absolute value of χ_P for $CeIr_2$ is more than 8 times larger than that of $LaIr_2$, which implies that the larger density of states at the Fermi level due to the 4*f*-electrons. Using the χ_P and the Sommerfeld coefficient γ = 28 mJ/(K^2mol), we can estimate the Wilson ratio $R_W = \frac{\pi^2 k_B^2}{3\mu_B^2}\frac{\chi_P}{\gamma}$, which is the measure of electronic correlations, to be $R_W \sim 1.5$. This value is slightly smaller than $R_W \sim 2$ of the typical heavy fermion

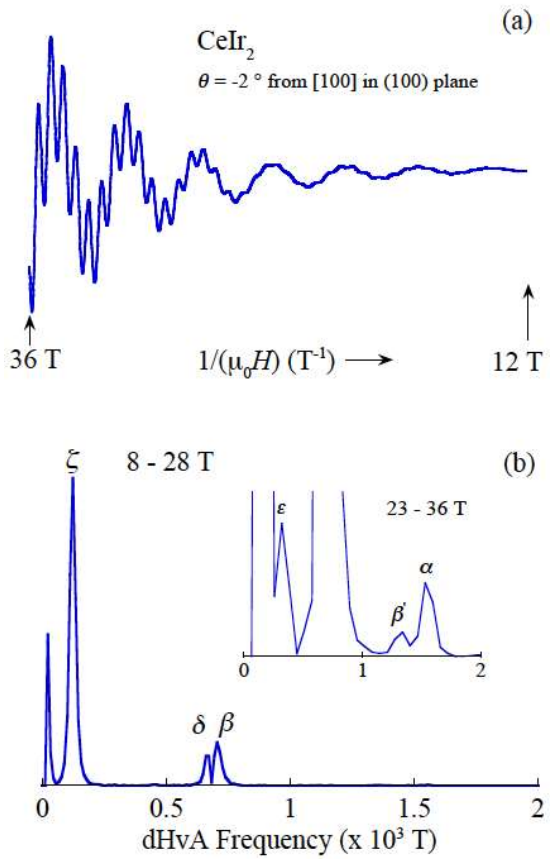

Fig. 4. (Color online) (a) Typical dHvA oscillations for field angle at $\theta = -2°$ from [100] in (100) plan and (b) the corresponding fast Fourier transformation (FFT) spectra in $CeIr_2$. The inset of (b) shows the FFT spectra between 23 and 36 T.

systems.[13)]

Next, we show the results of dHvA experiments on $CeIr_2$. Figures 4(a) and 4(b) show the typical dHvA oscillation for field angle at $\theta = -2°$ from [100] in (100) plan and the corresponding fast Fourier transformation (FFT) spectra, respectively. The dHvA frequency F, which is expressed as a unit of magnetic field, is proportional to the extremal cross-sectional area S_F of the Femi surface with the following relation $F = c\hbar S_F/(2\pi e)$.[14)]

Several dHvA-signals with F = (122-1560) T were observed as shown in Fig. 4(b), where the typical signals were labeled as α, β, β', ε, δ, and ζ. The amplitudes of signals β, δ, and ζ are relatively large, while those of α, β', and ε are small and only visible in the limited high filed ranges as shown in the inset of Fig. 4(b).

To investigate the Fermi surface (FS) topology, we measured the angular dependence of the dHvA frequency as shown in Fig. 5(a). The dHvA-frequency branches α and δ were observed over the whole angular ranges with weak angular dependences, indicating almost the spherical FSs, where the δ-branch corresponds to what we observed in our previous work.[3)] Thanks to the higher magnetic fields and the lower temperatures, we

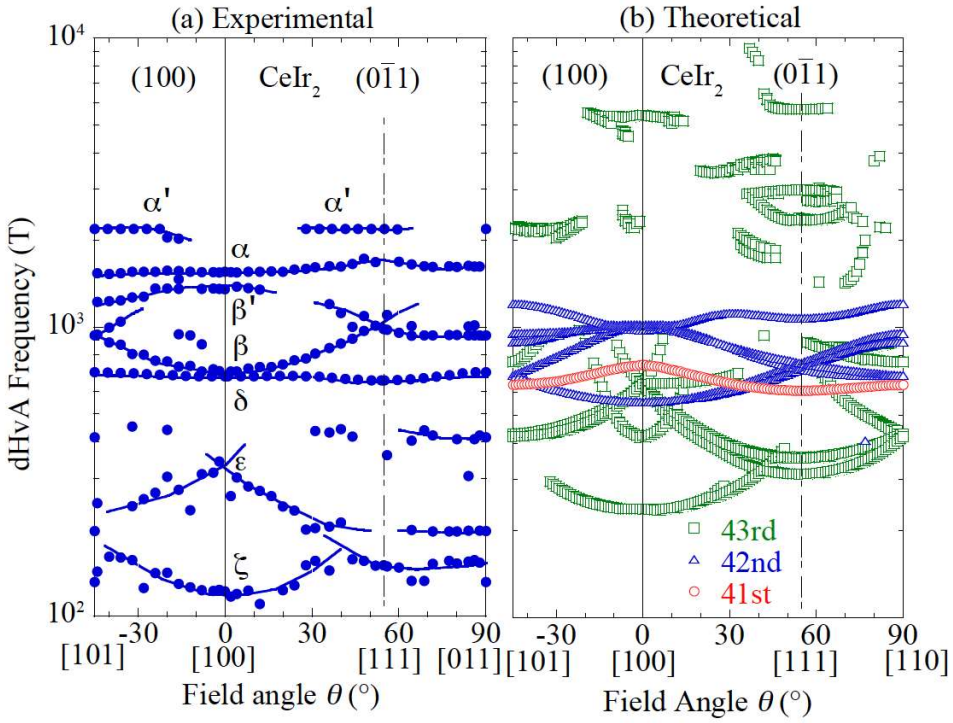

Fig. 5. (Color online) Comparison between (a) the experimental and (b) the theoretical angular dependences of the dHvA-frequencies in $CeIr_2$. Solid lines in (a) are guides to the eyes.

could observe several new dHvA-frequency branches in the present work. The branch α' was observed in the limited angular ranges at $\theta = -45 \sim -16°$ in (100) and $\theta = 28 \sim 59°$ in $(0\bar{1}1)$ with weak angular dependences. The branches β, β', ε, and ζ exhibit some specific angular dependences, whose possible origins will be discussed later.

In order to assign the origin of the dHvA-frequency branches, the band-structure calculations for $CeIr_2$ have been carried out based on a full-potential linearized augmented-plane-wave (FLAPW) method with in the local-density approximation (LDA). The resultant band structure and its density of states are shown in Figs. 6(a) and 6(b), respectively. The bands mainly consist of Ce-4*f* and Ir-5*d* bands and the FS consists of three sheets originating from the 41st-43rd bands as shown in Figs. 7(a)-7(c). The large

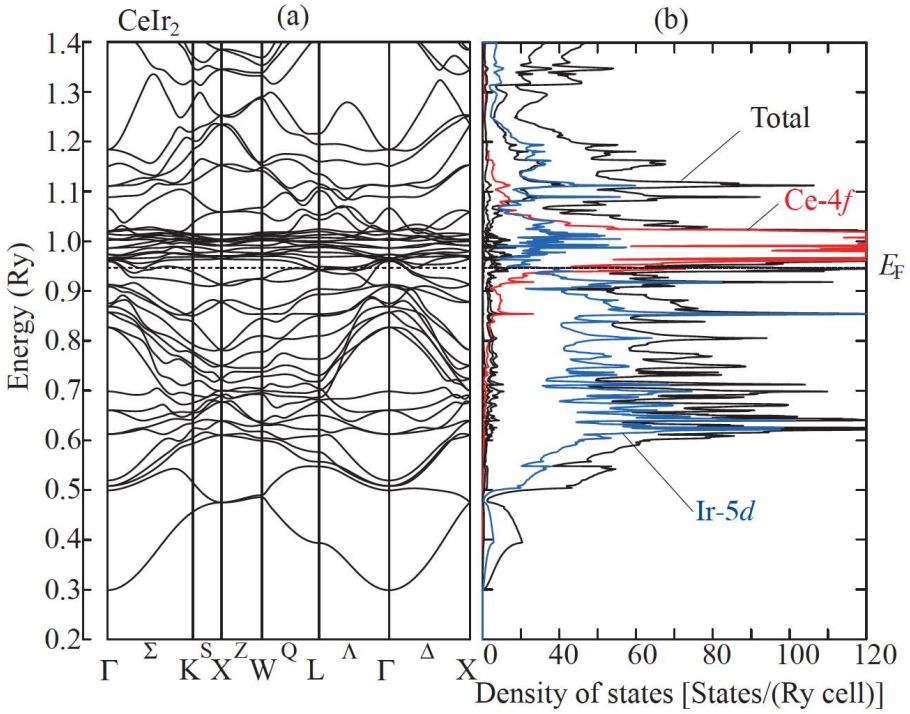

Fig. 6. (Color online) (a) Band structure and (b) its density of states of $CeIr_2$. Fermi energy is denoted by E_F.

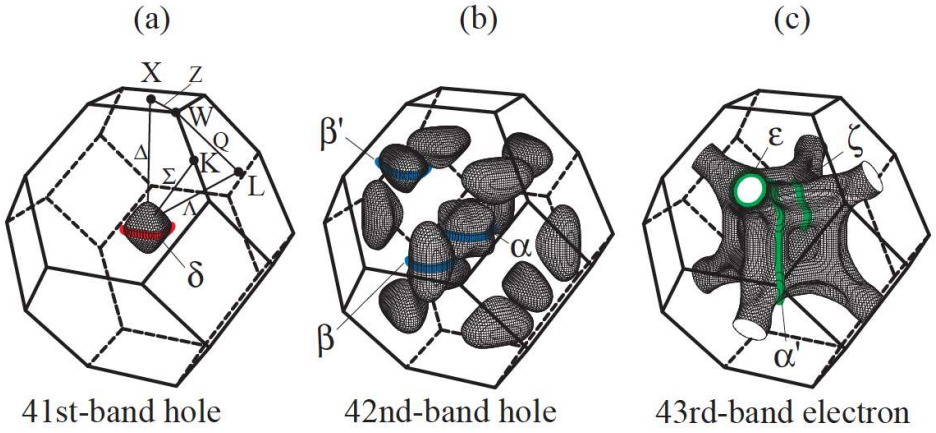

Fig.7. (Color online) Femi surface of $CeIr_2$. The Greek characters α, α', β, β', δ, ε, and ζ are corresponding to the observed dHvA branches as shown in Fig. 5(a). The other characters shown in (a) represent the specific points and axes of the first Brillouin zone (1st BZ), where the Γ point (not shown here) is the center of the BZ.

contribution of Ce-4*f* electrons is consistent with that $CeIr_2$ is a mixed valent compound. The total density of states (DOS) at Fermi energy E_F (= 0.94663 Ry) is 160.015 states/(Ry cell), which corresponds to the Sommerfeld coefficient of 13.87 mJ/(K^2mol). As shown in Fig. 7(a), the 41st-band constructs one hole FS centered at the Γ point of the first Brillouin zone (1st BZ), whose shape is almost spherical. The 42nd-band constructs hole sheets which consists of a rounded cube centered at the Γ point and twelve distorted ellipsoids which lie across the Σ axes as shown in Fig. 7(b). The 43rd-band constructs an electron sheet which is surrounding the Γ point and possessing eight open orbits along the <111> directions as shown in Fig. 7(c). This FS exhibits a hollow centered at the Γ point and the six windows along the <100> directions. $CeIr_2$ is a compensated metal with equal carrier number of electrons and holes because the primitive cell of the crystal structure consists of two molecules.

Hereafter let us consider the origin of the dHvA-frequency branches observed in the present experiments. The theoretical angular dependence of the dHvA-frequency obtained by the band-structure calculation is shown in Fig. 5(b). Compared with the theoretical angular dependence, it is evident that the branch δ is originated from the 41st-band hole FS. The branch α most likely corresponds to the round cube hole FS of the 42st-band although the absolute value of the dHvA frequency is about 1.5 times larger than that of the theoretical one. Assuming the spherical FSs, the FS volumes of branches δ and α are estimated to be 0.53% and 1.54% of the volume of the 1st BZ, respectively. Branches β and β' likely correspond to the ellipsoidal FSs of the 42st-band, whose extremal cross-sectional areas are almost degenerate for field along the [111] direction. The volume of ellipsoidal FSs estimated to be 19.86% of that of the BZ in total. Judging from the angular dependences, the branches α', ε, and ζ might originate from the 43rd-bands electron FS.

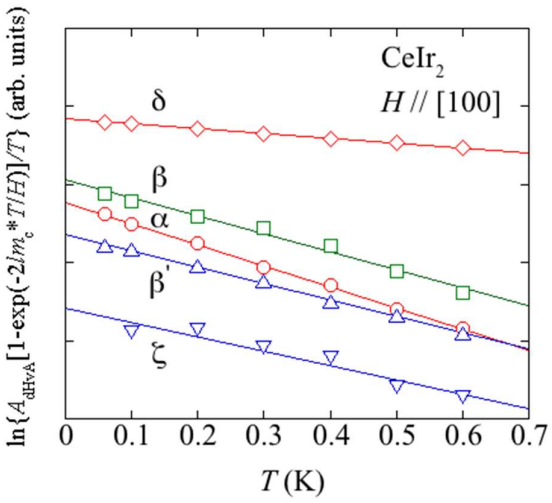

Fig. 8. (Color online) Temperature dependence of the dHvA amplitude A_{SdH} (mass plot) for α-, β-, β'-, δ-, and ζ-branches for field along H // [100] in $CeIr_2$. Solid lines represent linear fittings.

According to the Lifshitz-Kozevich formula,[14] the temperature dependence of the dHvA amplitude A_{dHvA} (magnitude of the FFT spectrum) is given by $\ln\{A_{dHvA}[1 - \exp(-2\lambda m_c^* T/H)]/T\} = -\lambda m_c^* T/H + \text{const.}$, where λ is a constant $\lambda = 2\pi^2 c k_B/(e\hbar)$ and the m_c^* is the cyclotron effective mass. From the temperature dependence of the dHvA amplitude (so-called mass plot) as shown in Fig. 8, we estimated the m_c^* for each dHvA frequency. The estimated m_c^*s compared with the results of band-structure calculation are summarized in Table I along with the dHvA frequencies. The experimental m_c^*s are not

Table I. dHvA frequency F and the corresponding cyclotron effective mass m_c^* in $CeIr_2$ for field along H// [100], H// [110], and H// [111] compared with the results of band structure calculation.

		Experimental		Theoretical		
Field direction	Branch	F ($\times 10^2$ T)	m_c^*/m_0	F ($\times 10^2$ T)	m_c^*/m_0	Band
[100]				54.05	5.792	43rd
	α	15.6	2.20±0.03	9.776	0.673	42nd
	β'	13.5	1.71±0.03	10.22	0.775	42nd
	β	7.58	1.9±0.1	5.556	1.593	42nd
	δ	6.75	0.83±0.01	7.446	0.490	41st
	ζ	1.22	1.3±0.1	2.365	1.150	43rd
[110]	α'	21.8	1.0±0.1	21.93	4.044	43rd
	α	15.4	2.14±0.05	12.10	0.971	42nd
	β'	12.0	-	8.902	2.548	42nd
	β	9.37	-	6.846	2.011	42nd
	δ	6.98	1.01±0.01	6.364	0.405	41st
	ζ	1.96	-	4.206	1.236	43rd
[111]				56.52	5.155	43rd
	α'	21.8	2.4±0.2	23.47	5.320	43rd
	β	9.84	-	1.078	0.800	42nd
	δ	6.54	0.87±0.01	6.071	0.385	41st
	ζ	1.49	-			

so large ranging from about 0.83 to 2.4 m_0 (m_0: rest mass of an electron), which are about 2 times larger than those of theoretical ones. The fact is consistent with the enhancement of the Sommerfeld coefficient; the experimental and theoretical Sommerfeld coefficients are (20~28) mJ/(K^{2}mol) and 13.78 mJ/(K^{2}mol), respectively. From the observed dHvA frequencies and their cyclotron effective masses, we estimate the electronic specific heat coefficient using the relation $\gamma = k_B^2 V m^* k_F/(3\hbar^2)$, where V is the molar volume, m^* is the effective mass, and k_F is the caliber of the Fermi sphere; $S_F = \pi k_F^2$. The estimated γ-values for α-, α'-, β(β')-, δ-, and ζ-branches are 0.8, 9.0, 6.5, 0.2, and 1.6 mJ/(K^{2}mol), respectively, and 18 mJ/(K^{2}mol) in total. This value is almost comparable to that estimated from the specific heat measurements. The band structure calculation predicted the dHvA frequency F = 5405 T with the largest m_c^* = 5.792 m_0 of the 43rd-band electron FS for H // [100], however, we did not observe the corresponding dHvA single in the present experiment. Considering the mass enhancement, the expected m_c^* for this dHvA frequency should be ~12 m_0, which might be observable if we could improve more the sample quality, that is future work.

Finally, we compare the typical physical quantities of $CeIr_2$ with those of $CeRu_2$ and $CeCo_2$ as shown in Table II,[3, 15-18] which might be helpful to understand the difference of those superconducting properties. Among these compounds, $CeRu_2$ exhibits the highest T_c of 6.3 K, which is even highest among all Ce-based intermetallic compounds. The most interesting feature of the superconducting properties is the possibility of an anisotropic *s*-wave superconducting gap, which was demonstrated by the nuclear magnetic resonance (NMR), [19,] the photoemission spectroscopy,[20] and more conclusively by the field angle

Table II. Comparison of superconducting and other physical quantities in CeX_2 (X = Co, Ru, and Ir). The parenthesis numbers beside to the values mean the references.

Physical quantity	$CeIr_2$	$CeRu_2$	$CeCo_2$
T_c (K)	0.3	6.3 [15]	1.5 [17]
$\mu_0 H_{c2}$ (T)	0.23	5.2 [15]	0.22 [18]
γ (mJ/K^{2}mol)	28 [3]	27 [15]	36 [17]
χ_P (X10^{-4} emu/mol)	5.9	7 [16]	10 [17]
Θ_D (K)	232 [3]	120 [15]	200 [17]
λ_{ep}	0.39	0.80	0.59

resolved specific heat measurements.[21] $CeCo_2$ also exhibits relatively higher T_c of 1.5 K among Ce-compounds despite consisting magnetic element Co. This compound also reported as an anisotropic *s*-wave superconductor from the NMR measurements,[22] and the ferromagnetic spin fluctuation was considered as the gap anisotropy from the specific heat measurements.[17] It is evident that the large variation of T_c in CeX_2, i.e., 0.3 ~ 6.3 K, although the γ-values are not so much different among these compounds. This fact is somewhat curious considering the BCS theory; T_c is given by $T_c = 1.14\Theta_D \exp\left[\frac{-1}{N(0)V}\right]$, where $N(0)$ is the density of states at the Fermi energy and V is the pairing potential arising from the electron-phonon interaction. Since the Debye temperature Θ_D of $CeRu_2$ is about two times smaller than that of $CeIr_2$ while the T_c is more than one order larger. The large variation of T_c can be understood by the difference of those strength of electron-phonon couplings. By using a McMillan formula mentioned above, we can estimate the electron-phonon coupling constants for $CeRu_2$ and $CeCo_2$ to be 0.80 and 0.59, respectively, which are comparable with the medium value of that of pure Nb ($\lambda_{ep} = 0.82$). On the other hand,

$\lambda_{ep} = 0.39$ for $CeIr_2$ is closed to that of pure Al ($\lambda_{ep} = 0.38$) which is a typical weak-coupling BCS-type superconductor. However, a question remains what is the microscopic mechanism for the large difference of λ_{ep} depending on the X element.

It is interesting to discuss from the viewpoint of difference of band structures, especially from the role of 4*f*-electrons, because all these compounds are situated in the valence fluctuation regime and the 4*f*-electron's contribution is expected to be important for the superconductivity. The systematic band structure calculations for CeX_2, including non-superconducting $CeRh_2$ above 0.2 K, were performed by Tanaka et al.[21] The comparison of the DOS at the vicinity of E_F along with $CeIr_2$ are shown in Fig.9. The remarkable points of the electronic structures are summarized as follows. For all CeX_2, the contributions of 4*f*-compornents of Ce to DOS (4*f*-DOS) are large at E_F, indicating the large contribution to the band structures. However, the shape of 4*f*-DOS and its relative position to E_F are highly different among these compounds. The main peak of 4*f*-DOS for $CeRu_2$ is lying slightly above E_F ~0.007 Ry, while the small peak of 4*f*-DOS exists below E_F around ~0.04 Ry. On the other hand, the main peak of 4*f*-DOS of $CeCo_2$ is lying far from E_F above ~0.03 Ry and the small peak of 4*f*-DOS exists just below E_F. From the band structure calculations, Tanaka et al. suggested that the shape of 4*f*-DOS and the relative position to E_F is important for the mass enhancemen. For $CeIr_2$, the total DOS at E_F is almost the same as those of $CeRu_2$ and $CeCo_2$, however, the shape is highly different; the large peaks of 4*f*-DOS exist in both sides of the vicinity of E_F, which is rather similar to that of no-superconducting $CeRh_2$. Such a difference of the band structure and the possible hybridization effect between Ce 4*f*- and X *d*-electrons may be

responsible for the difference of the superconductivity in CeX_2.

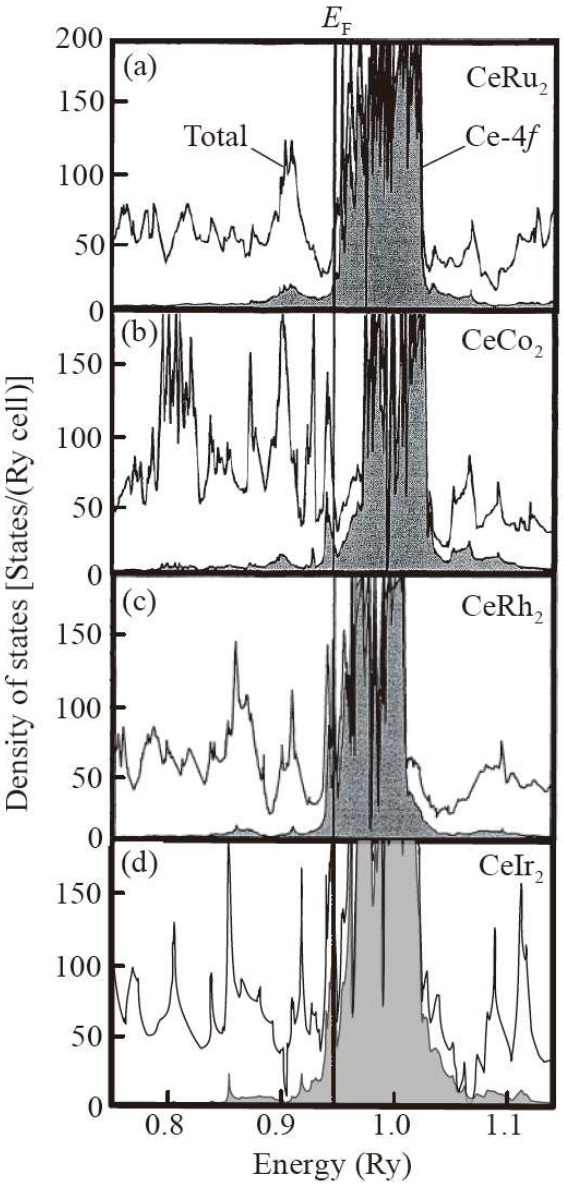

Fig. 9. Comparison of calculated density of states (DOS) at the vicinity of E_F for (a) $CeRu_2$, (b) $CeCo_2$, (c) $CeRh_2$, and (d) $CeIr_2$. Total DOS and the partial DOS for the 4*f*-compormnent are shown by solid lines and shadow areas, respectively. The DOS for $CeRu_2$, $CeCo_2$, and $CeRh_2$ are drawn from Ref. 23.

4. Summary

We measured the electrical resistivity, the magnetic susceptibility, and the dHvA effect to investigate the electronic and the superconducting properties in $CeIr_2$. The superconducting H–T phase diagram was constructed by the electrical resistivity measurements under the magnetic fields, where the critical temperature T_c = 0.3 K and the upper critical filed $\mu_0 H_{c2}$ = 0.23 T were determined. In the present work, the superconductivity can be explained by the weak-coupling BCS theory with the electron-phonon coupling constant $\lambda_{ep} = 0.39$. The magnetic susceptibility is nearly constant at high temperatures suggesting Pauli paramagnetism. Combined with the γ-value of 28 mJ/K^{2}mol and the Pauli paramagnetic susceptibility $\chi_P = 0.71 \times 10^{-4}$ emu/mol, $CeIr_2$ is a weakly correlated electron system. From the dHvA effect measurements we observed the dHvA branches with the frequencies of F = (122 ~ 2180) T and the effective masses of m_c^* = (0.83~2.4)m_0, which were reasonably well explained by the band structure calculation. The large variation of T_c in CeX_2 were discussed on the basis of differences of the band structures at the vicinity of E_F.

Acknowledgment

This work was partly supported by JSPS KAKENHI Grants Nos. JP15H05882, JP15H05884, JP15H05885, 18H04320, and 18H04321 (J-Physics).

*E-mail: sugawara@crystal.kobe-u.ac.jp

1) V. B. Compton and B. T. Matthias, Acta Cryst. **12**, 651 (1959).

2) H. Sugawara, T. Yamazaki, J. Itoh, M. Takashita, T. Ebihara, N. Kimura, P. Svoboda, R. Settai, Y. Onuki, H. Sato, S. Uji, and H. Aoki, J. Phys. Soc. Jpn. **63**, 1502 (1994).
3) K. Omasa, E. Matsuoka, H. Kotegawa, H. Tou, A. Nakamura, Y. Homma, D. Aoki, D. Satoh, M. Yoshida, T. Takeuchi, H. Harima, and H. Sugawara, JPS Conf. Proc. **30**, 011130 (2020).
4) D. Satoh, T. Shibuya, H. Ogata, M. Tanaka, H. Ikeura-Sekiguchi, R. Kuroda, M. Yoshida, H. Sugawara, and H. Toyokawa, Jpn. J. Appl. Phys. **58**, SIIB10 (2019).
5) T. Maehira, Y. Tatetsu, H. Teruya, and E. Sakai, J. Phys. Soc. Jpn, **81**, SB012 (2012).
6) K. Omasa, E. Matsuoka, H. Kotegawa, H. Tou, A. Nakamura, Y. Homma, D. Aoki, D. Satoh, M. Yoshida, T. Takeuchi, H. Harima, and H. Sugawara, JPS Conf. Proc. **29**, 012012 (2020).
7) K. Kadowaki and S. B. Woods, Solid State Commun. **58**, 507 (1986).
8) Y. J. Sato, A. Nakamura, Y. Shimizu, A. Maurya, Y. Homma, D. Li, F. Honda, and D. Aoki, J. Phys. Soc. Jpn., **87**, 053704 (2018).
9) T. H. Geballk, B. T. Matthias, B.V. Compton, E. Corenzwit, G. W. Hull, and L. D. Longinotti, Phys. Rev. **137**, 331 (1965).
10) L. W. McMillan, Phys. Rev. **167**, A119 (1968).
11) E. Helfand and N. R. Werthamer, Phys. Rev. **147**, 288 (1966).
12) N. R. Werthamer, E. Helfand, and P. C. Hohenberg, Phys. Rev. **147**, 295 (1966).
13) L. A. Lee, T. M. Rice, J. W. Serene, L. J. Sham, and J. W. Wilkins, Comments on Condensed Mater Physics. **12**, 99 (1986).
14) D. Shoenberg, *Magnetic Oscillations in Metals* (Cambridge University Press, Cambridge, 1984) p. 22.
15) M. Hedo, Y. Inada, E. Yamamoto, Y. Haga, Y. Onuki, Y. Aoki, T. D. Matsuda, H. Sato, and S. Takahashi, J. Phys. Soc. Jpn. **67**, 272 (1998).
16) H. Sugawara, H. Sato, T. Yamazaki, N. Kimura, R. Settai, and Y. Onuki, J. Phys. Soc.

Jpn. **64**, 4849 (1995).
17) Y. Aoki, T. Nishigaki, H. Sugawara, and H. Sato, Phys Rev. B **55**, 2768 (1997).
18) H. Sugawara, O. Inoue, Y. Kobayashi, H. Sato, T. Nishigaki, Y. Aoki, H. Sato, R. Settai, and Y. Onuki, J. Phys. Soc. Jpn. **64**, 3639 (1995).
19) H. Mukuda, K. Ishida, Y. Kitaoka, and K. Asayama, J. Phys. Soc. Jpn. **67**, 2101 (1998).
20) T. Kiss, F. Kanetaka, T. Yokoya, T. Shimojima, K. Kanai, S. Shin, Y. Ōnuki, T. Togashi, C. Zhang, C. T. Chen, and S. Watanabe, Phys. Rev. Lett. **94**, 057001 (2005).
21) S. Kittaka, T. Sakakibara, M. Hedo, Y. Ōnuki, and K. Machida, J. Phys. Soc. Jpn. **82**, 123706 (2013).
22) K. Ishida, H. Mukuda, Y. Kitaoka, K. Asayama, H. Sugawara, Y. Aoki, and H. Sato, Physica B **237-238**, 304 (1997).
23) S. Tanaka, H. Harima, and A. Yanase, J. Phys. Soc. Jpn. **67**, 1342 (1998).